Earth and Planetary Science Letters 595 (2022) 117786

Contents lists available at ScienceDirect

Earth and Planetary Science Letters

www.elsevier.com/locate/epsl

How strongly do plumes influence Pacific seamount distribution?

Yanghui Zhao [a,*], Bryan Riel [b,c], Gillian Foulger [d,e], Weiwei Ding [a,f,**]

[a] Key Laboratory of Submarine Geosciences, Second Institute of Oceanography, Ministry of Natural Resources, Hangzhou 310012, China
[b] School of Earth Sciences, Zhejiang University, Hangzhou 310027, China
[c] Department of Earth, Atmospheric and Planetary Sciences, Massachusetts Institute of Technology, Cambridge, MA 02139, USA
[d] Department of Earth Sciences, Durham University, Durham DH1 3LE, UK
[e] Institute of Marine Geodynamics, College of Marine Geosciences, Ocean University of China, Qingdao 266100, China
[f] School of Oceanography, Shanghai Jiao Tong University, Shanghai 20030, China

ARTICLE INFO

Article history:
Received 6 April 2022
Received in revised form 16 August 2022
Accepted 17 August 2022
Available online 29 August 2022
Editor: H. Thybo

Dataset link: https://topex.ucsd.edu/WWW_html/srtm15_plus.html

Dataset link: https://www.ngdc.noaa.gov/mgg/sedthick/

Dataset link: https://doi.org/10.5281/zenodo.5716540

Keywords:
intraplate volcanism
seamount volume
mantle plume
Pacific plate
Gaussian Process regression

ABSTRACT

Seamounts are submarine volcanoes postulated to be formed either by hot mantle plumes rising from the deep mantle or by shallow, plate-related processes. However, the relative importance of these two mechanisms has not hitherto been quantified. In this study, applying Gaussian Process regression to reconstruct irregular seamount topography above and under the sedimentary layer, we calculate an accurate map of volcanism distribution within the Pacific plate. We find that previous erupted volumes have been underestimated by 75% on average. Our results show that (1) the total erupted volume postulated to be plume-related makes up only 18% of total Pacific intraplate volcanism, and (2) the volume statistics for plume-related seamounts and those along the Large Low-Shear-Velocity Province margins are nearly indistinguishable from the rest of the intraplate seamounts. We conclude that proposed plumes account for only a minority of the volume of intraplate volcanism in the Pacific plate, implying that shallow rather than deep processes are dominant.

1. Introduction

Classical plate tectonic theory can effectively explain the volcanism along or near the plate boundaries, such as mid-ocean ridges and subduction zones (Wilson, 1966). However, an assumed rigid lithosphere cannot explain the occurrence of massive active volcanoes away from plate boundaries. To explain intraplate volcanism, two classes of melt-generating mechanisms, mantle plumes (*e.g.*, Morgan, 1971) and non-plume processes (i.e. tectonic plate processes, *e.g.*, Anderson, 2000) have been proposed.

The discovery of the northwest-oriented lineament of the Hawaiian archipelago led to the birth of the mantle plume model (Morgan, 1971; Wilson, 1963). The mantle plume model proposes an upwelling of abnormally hot material that rises from the lowermost mantle in the form of narrow conduits and produces large volumes of volcanism on the surface (Coffin and Eldholm, 1994; Morgan, 1971; Sleep, 1990; Wilson, 1963). Seismic studies suggest that current active "hotspots" (i.e. the proposed surface locations of active mantle plumes) usually appear above thinner mantle transition zones (Courtier et al., 2007) and the margins of Large Low-Shear-Velocity Provinces (LLSVPs) in the lower mantle (Lau et al., 2017; Torsvik et al., 2010; Zhao et al., 2015). However, due to the difficulty of magma volume calculation, the quantity of magma brought by mantle plumes to the surface has not yet been assessed.

In order to explain the occurrence of magma away from hotspots, some volcanism has been attributed to lateral flow of plume material (Phipps Morgan et al., 1995; Sleep, 1997). Whilst of interest, this hypothesis is not easily testable and could potentially be used to explain any intraplate volcanism, in particular where information on local lithosphere thickness is absent. Given

* Corresponding author.
** Corresponding author at: Key Laboratory of Submarine Geosciences, Second Institute of Oceanography, Ministry of Natural Resources, Hangzhou 310012, China.
E-mail addresses: zhaoyh@sio.org.cn (Y. Zhao), wwding@sio.org.cn (W. Ding).

https://doi.org/10.1016/j.epsl.2022.117786

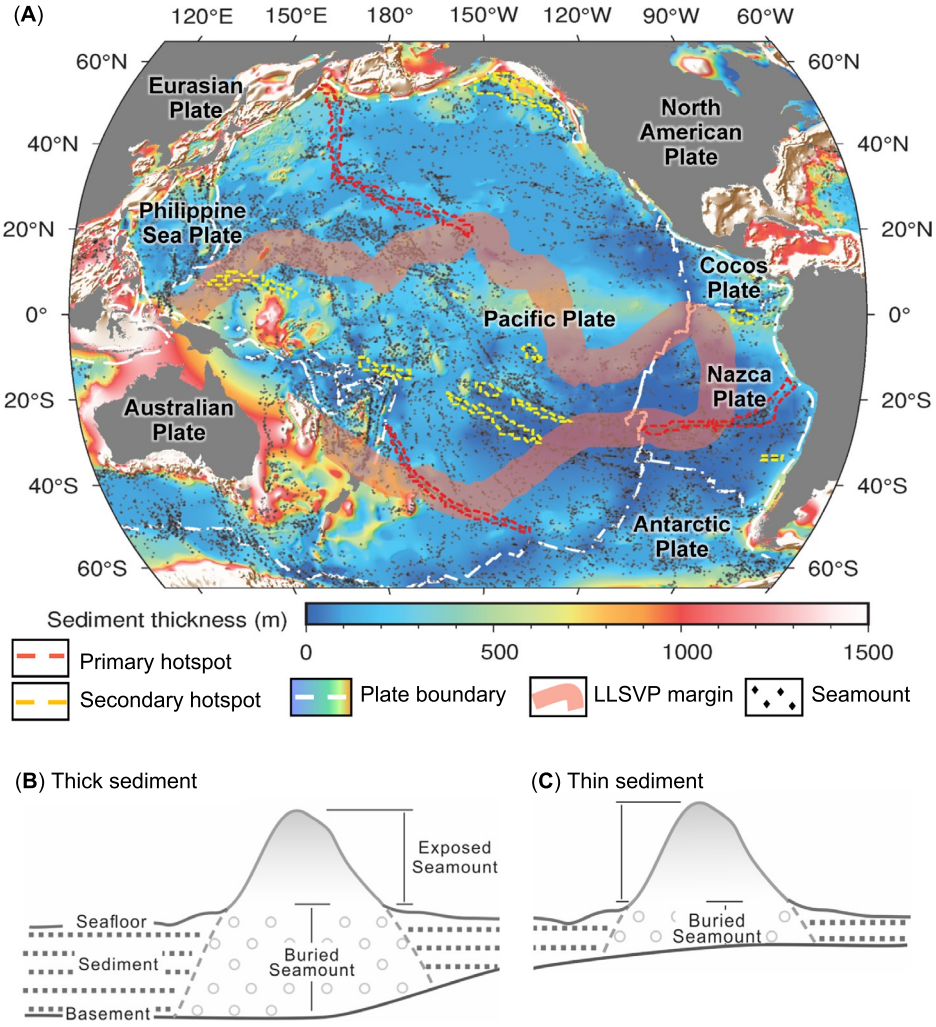

Fig. 1. Seamount database of Kim and Wessel (2011) plotted on the sediment thickness model of Straume et al. (2019). The sediment thickness map was drawn using the Generic Mapping Tools (Wessel et al., 2019). Red dashed lines delimit "primary hotspots", proposed to originate from the lowermost mantle. Yellow dashed lines delimit "secondary hotspots", proposed to arise from the mantle transition zone (Courtillot et al., 2003). White dashed lines denote plate boundaries. Red shading marks 1000-km-wide LLSVP margin as defined by Torsvik et al. (2006). Thick sediments cloak much more seamount volume than thin sediments.

this, it is beyond the remit of the present paper to attempt further quantification of this potential effect.

Other studies propose that shallow, non-plume processes cause widespread intraplate volcanism, such as intraplate lithospheric extension (Anderson, 2000; Fairhead and Wilson, 2005; Foulger and Natland, 2003), plate flexural deformation (Hieronymus and Bercovici, 1999), thermal contraction (Gans et al., 2003; Stuart et al., 2007), plate-boundary forces such as slab pull and ridge push (Hirano et al., 2006), sub-lithospheric processes generating upwelling flow via density heterogeneities (Ballmer et al., 2007; Bonatti and Harrison, 1976), and asthenospheric shearing coupled with viscosity heterogeneities (Conrad et al., 2011, 2010). These non-plume mechanisms challenge classic plate tectonic theory and the mantle plume model. It is debated whether deep mantle processes dynamically supply intraplate volcanism since it was proposed 50 years ago. We contribute to this debate by quantifying the conceivable relative importances of the two melt-generating mechanisms in a way that has not been attempted before.

In this paper we compare the geographic distribution of intraplate volcanism, both proposed and not proposed to have been produced by plumes. The Pacific plate is the best region for our study because it contains abundant seamounts far from the plate boundaries and is underlain by the largest LLSVP (Fig. 1). Three outcomes are possible, and have the following implications for mantle geodynamics:

- Outcome 1: Most seamount volume is attributed to mantle plumes implying that, within plate interiors, erupted melt volumes are consistent with whole-mantle convection bringing material up from the lower mantle.
- Outcome 2: Most seamount volume has not been attributed to mantle plumes implying that, within plate interiors, volcanism is dominated by upper-mantle convection driven by non-plume processes.
- Outcome 3: Roughly equal proportions are found for plume- and non-plume-related volcanism, supporting both processes making an approximately equal contribution to Pacific intraplate volcanism.

A number of studies have mapped seamount locations and estimated their distributions globally (Craig and Sandwell, 1988; Kim and Wessel, 2011; Kitchingman et al., 2007; Wessel, 2001; Yesson et al., 2011). The database of Kim and Wessel (2011) models seamounts as ideal elliptical cones and includes ellipse major-axis, minor-axis and height in order to estimate seamount volume. However, the accuracy of estimated seamount volumes is highly influenced by how well idealized geometries represent observed

seamounts, which can be highly irregular in shape (Zhao et al., 2020). Furthermore, the calculated volume can be seriously underestimated by thick sediment coverage obscuring a significant fraction of the seamount by blanketing its base (Wessel et al., 2010) (Fig. 1). Our study advances previous seamount volume estimates by (1) taking account of irregular seamount topography, and (2) correcting for the varying sediment thicknesses that obscure the bases of the seamounts.

One critical problem is to separate the seamounts proposed, and not proposed, to have been fed by plumes. Within the Pacific plate, different seamount chains have been attributed to plumes by different authors (Courtillot et al., 2003; Morgan and Morgan, 2007; Sleep, 1990; Torsvik et al., 2006). We categorize seamounts based on these previously published lists. For the main text, we use the list of Courtillot et al. (2003). We also study seamounts along the Pacific LLSVP margin to investigate seamount generation proposed to be linked to plumes guided by the LLSVP margins (Torsvik et al., 2006).

2. Data and methods

2.1. Data and general approach

To quantify seamount volume over the Pacific plate, we use the SRTM15+V2.0 global bathymetry grid (Tozer et al., 2019). Bathymetry is provided at a spatial sampling of 15 arc s (~500 m) and is derived from a combination of satellite altimetry and multi-beam and single-beam shipboard measurements over selected areas. We first apply a white top-hat filter to the bathymetry data to isolate short-wavelength seamount topography above long-wavelength seafloor (Zhao et al., 2020). We validate the extracted seamount locations with the database of Kim and Wessel (2011). Subsequently, we apply large-scale Gaussian Process regression to the top-hat results to determine seamount structure above the seafloor in order to extrapolate structure beneath the sediment to the basaltic basement (i.e., the top of the oceanic crust) (Supplementary Figs. S1-S3). Local sediment thickness is extracted from GlobSed-V3 (Straume et al., 2019). Finally, we map the spatial distribution of seamount volume on the Pacific plate by calculating a volcanic equivalent layer thickness (VELT), and examine the relationship between volume and seafloor age (Seton et al., 2020). In the following, we further expand on the algorithmic details of each step of the workflow.

2.2. Reconstruction of above-basement topography

The first step in our workflow is to isolate irregular seamount topography above the seafloor. To that end, we utilize a top-hat transform, which is an image processing technique that picks small elements from 1D signals and 2D images (Meyer, 1979). For example, for 2D images, the white top-hat function allows the extraction of peaks in a gray-tone image that are smaller than some reference structuring element (Matheron and Serra, 1988; Vogt and Del Valle, 1994). For digital elevation models (DEMs), this operation permits extraction of positive relief features with specific size and shape properties (Tripathi et al., 2000). Thereby, only the information for the higher elevation peaks with wavelengths smaller than the structuring element are kept. The white top-hat filter has been successfully applied to isolate seamount topography above the seafloor in the South China Sea while removing oceanic plateaus and fracture zone scarps (Zhao et al., 2020).

The next step in our workflow is to extrapolate the above-seafloor seamount topography to the depth of the basaltic basement, where basement depth is determined by local sediment thickness. This extrapolation is only performed on seamounts that have their bases partially obscured by sediment (i.e., not seamounts that are completely buried) since here we only use bathymetry data. To that end, we first apply a Gaussian Process (GP) regression to the above-sediment bathymetry as computed by the white top-hat transform. A GP represents a distribution over functions by approximating the distribution with a mean function and a covariance function. In this work, the distribution of functions of interest is the distribution of bathymetry, $h(x)$, above some reference plane (the basement) and throughout a spatial domain indexed by the coordinates x. For the purposes of introducing GPs, we assume that our analysis area is relatively narrow (*e.g.*, tens of kilometers) such that the reference plane is constant throughout. The following discussion closely follows that of (Rasmussen, 2003). Our aim is to draw realistic samples of bathymetry from a GP approximation:

$$\mathrm{h}\left(\mathrm{x}\right) \sim \mathcal{GP}\left(m\left(x\right), k\left(x, x'\right)\right), \tag{1}$$

where $m(x)$ is the mean function and $k(x, x')$ is the covariance function describing the covariance of bathymetry between points x and x'. More concretely, given vectors of length N of bathymetry and coordinates, $\boldsymbol{h}$, $\boldsymbol{x} \in \mathbb{R}^{\mathrm{N}}$, we aim to construct an approximating Gaussian distribution:

$$\boldsymbol{h} \sim \mathcal{N}\left(\boldsymbol{m},\ \boldsymbol{K}\right), \tag{2}$$

where $\boldsymbol{m} \in \mathbb{R}^{\mathrm{N}}$ is now the mean vector and $\boldsymbol{K} \in \mathbb{R}^{N \times N}$ is the covariance matrix for a multivariate Gaussian distribution. Note, we adopt the vector notation as $m_i = m(x_i),\ i = 1, \ldots, N$, and $K_{ij} = k(x_i, x_j),\ i = 1, \ldots, N$ and $j = 1, \ldots, N$. The covariance matrix $\boldsymbol{K}$ is thus constructed by evaluating the covariance function $k(x, x')$ at unique combinations of the coordinates in $\boldsymbol{x}$. There are a number of classes of covariance functions (also referred to as kernels) commonly used, and each has different characteristic roughness, shape, lengthscale, periodicity, etc. in order to model a diverse range of functions. Here, we use the radial basis function (RBF) kernel:

$$\mathrm{k}\left(x, x'\right) = A exp\left(-\frac{\left(x - x'\right)^2}{2\sigma^2}\right), \tag{3}$$

which is described by the hyperparameters A and σ, which are the amplitude and lengthscale, respectively, of the kernel. For our purposes, the kernel amplitude controls the amount of modeled vertical variation in bathymetry while the lengthscale controls its roughness. Note that the kernel has an x^2 dependency, which is consistent with the gravity-derived bathymetry that nominally follows Newton's law of gravity. The RBF kernel is thus the optimal kernel choice for modeling the statistics of the SRTM15+V2.0 bathymetry used in this work.

To formulate the prediction equations for the GPs, we first designate the vectors of the spatial coordinates, $\boldsymbol{x}$, and above-seafloor topography, $\boldsymbol{h}$, as the GP inputs and outputs, respectively. These vectors comprise the entire training data and are populated by the outputs of the white top-hat transform. Note that only above-seafloor topography over a certain threshold is included in the training data (see workflow at the end of this section). The inputs for prediction, i.e. the test data inputs, consist of the spatial coordinates, $\boldsymbol{x}^* \in \mathbb{R}^{\mathrm{M}}$, not included in the training data. Nominally, these coordinates correspond to regions where above-seafloor topography is below the height threshold used for the training data. Then, to predict bathymetry, $\boldsymbol{h}^* \in \mathbb{R}^{\mathrm{M}}$, at these coordinates, we use the joint distribution:

$$\begin{bmatrix} \boldsymbol{h} \\ \boldsymbol{h}^* \end{bmatrix} \sim \mathcal{N}\left(\begin{bmatrix} \boldsymbol{m} \\ \boldsymbol{m}^* \end{bmatrix}, \begin{bmatrix} \boldsymbol{K} & \boldsymbol{K}^* \\ \boldsymbol{K}^{*T} & \boldsymbol{K}^{**} \end{bmatrix}\right), \tag{4}$$

where we use the notation $K^*_{ij} = k(x_i, x^*_j)$, $i = 1, \ldots, N$ and $j = 1, \ldots, M$, and $K^{**}_{ij} = k(x^*_i, x^*_j)$, $i = 1, \ldots, M$ and $j = 1, \ldots, M$. Using standard rules for conditional Gaussians, we can then write the posterior predictive distribution from the joint distribution as:

$$\mathbf{h}^* \mid \mathbf{h} \sim \mathcal{N}\left(\mathbf{m}^* + \mathbf{K}^{*\mathrm{T}}\mathbf{K}^{-1}\left(\mathbf{h} - \mathbf{m}\right), \mathbf{K}^{**} - \mathbf{K}^{*\mathrm{T}}\mathbf{K}^{-1}\mathbf{K}^*\right). \quad (5)$$

Therefore, for given values of the kernel hyperparameters, the covariance matrices and vectors can be evaluated at the training and prediction coordinates in order to compute the posterior mean and covariance matrix for the bathymetry at the prediction coordinates.

The hyperparameter values can significantly influence the smoothness of the predicted bathymetry. We aim for a predictive distribution that does not overfit the training data and generalizes well to unseen prediction coordinates. To that end, we perform a non-linear optimization for the hyperparameters by maximizing the log marginal likelihood for the training data:

$$\log p\left(\mathbf{h} \mid \mathbf{x}, A, \sigma\right) = -\frac{1}{2}\log|\mathbf{K}| - \frac{1}{2}\left(\mathbf{h} - \mathbf{m}\right)^T \mathbf{K}^{-1}\left(\mathbf{h} - \mathbf{m}\right) - \frac{N}{2} log\left(2\pi\right). \quad (6)$$

The final key algorithmic choice involves the value of the mean function at the training and prediction coordinates. Here, we set the mean function to be zero at all coordinates. In addition to simplification of the above equations, this encourages the bathymetric predictions to trend towards zero away from the training data. Within our context of recovery of bathymetry covered by sediments, this design choice is mathematically equivalent to placing the basaltic basement as the reference plane ($h = 0$), and the spatial pattern at which the predicted topography reaches that reference plane is informed by the covariance structure represented by the kernel and the optimized hyperparameters.

In order to scale this procedure to the entire Pacific plate, we divide the Pacific region into square tiles with side lengths of 6 degrees with a 0.5 degree overlap between each tile. For each tile, we independently implement the following workflow: (1) extract bathymetry from the SRTM15+V2.0 grid (Tozer et al., 2019); (2) apply a white top-hat filter (using a disk structuring element with a radius of 20 km) in order to isolate short-wavelength bathymetry from the long-wavelength seafloor; (3) add bias computed from a 2D bilinear ramp associated with the local sediment thickness, extracted from GlobSed-V3 (Straume et al., 2019); (4) construct GP training data by randomly selecting bathymetry points above a height-above-seafloor threshold (500 m); (5) perform GP hyperparameter optimization; and (6) predict bathymetry at all points within the tile. In step (2), the short-wavelength bathymetry values are referenced above the seafloor. Therefore, the purpose of step (3) is to bias the observed bathymetry to be above the basaltic basement, which is now the reference plane. Step (6) is the final prediction step where the below-sediment bathymetry is extrapolated using the optimized kernel hyperparameters, along with associated uncertainties computed from the diagonal of the posterior predictive covariance matrix. A more rigorous uncertainty analysis would likely incorporate uncertainties associated with the sediment thickness grid. Nevertheless, we can utilize the GP uncertainties as a qualitative check on the bathymetry predictions. Since the GP mean functions are set to zero, we limit spurious bathymetric predictions between seamounts that are separated by large distances within the tile.

In summary, we use a white top-hat filter to isolate irregular seamount topography from the seafloor and GP regression to extrapolate the base of the seamount that is partially obscured by sediment. These results are used to obtain the spatial distribution of above-basement seamount volume over the entire Pacific, thus permitting a comparison of the seamount volume between proposed plume and non-plume volcanism, as described in the next section.

2.3. Quantification of seamount volume distribution

Following Conrad et al. (2017), we map the spatial distribution of seamount volume on the Pacific plate by calculating a volcanic equivalent layer thickness (VELT) using a moving window of 300 × 300 km (Fig. 2). For computing the VELT grid for the entire Pacific region we assemble the tile predictions of predicted bathymetry above the basement and average the values in the overlap regions to minimize tile boundary artifacts. We use an identical procedure for assembling the VELT uncertainty grid where uncertainties are computed with simple propagation of uncertainties of the bathymetric values.

To further assess the spatial distribution of seamount volume, we examine the relationship between volume and seafloor age (Seton et al., 2020). Seafloor age increases with distance from the spreading center (Supplementary Fig. S4), thus providing a convenient context to compare spatial and temporal distributions of seamount volume. We divide our VELT grids into bins of equal age (∼4 Ma) and compute a mean VELT, $\overline{v}$, for each age bin:

$$\overline{v} = \frac{\sum_i^N \mathrm{VELT}_i}{N}, \quad (7)$$

where VELTi is the VELT value for i-th grid cell, and N is the total number of grid cells for the given age bin.

3. Seamount volume distribution on the Pacific plate

3.1. Spatial distribution of seamount volume

The greatest volcanic volumes are located in the western Pacific, where VELT can reach up to 700 m on the old oceanic crust (Figs. 2A and 2B). The asymmetric distribution of VELT between the eastern and western Pacific is consistent with earlier findings that the largest seamounts lie on the oldest crust (Conrad et al., 2017; Kim and Wessel, 2011; Wessel, 1997) (Fig. 2C). Comparison of VELT above the seafloor with VELT above the basaltic basement (i.e., adding volume buried by sediment) shows that the largest corrections for sediment cover occur for the areas with larger VELT in general (Fig. 2D). This trend is consistent with a straightforward geometric reasoning that larger seamounts will have larger absolute volumes covered by sediment. Areas with thick VELT are mainly along the large seamount chains with various ages of activity, including currently active seamounts (Fig. 2E). High values of VELT are associated both with chains attributed to plumes (e.g., Hawaii and Samoa) and to non-plume processes (e.g., the Tokelau chain, the Gilbert chain, the Line islands and scattered seamounts on the oldest crust) (Courtillot et al., 2003) (Fig. 2E). After removing seamounts classified as plume-related by Courtillot et al. (2003) and re-computing VELT, we find that the change in the spatial distribution of VELT is minor–the old seafloor in the western Pacific still has the greatest volume of intraplate volcanism (Fig. 2F).

Since the bathymetric grid (SRTM15+V2.0) is constructed using a combination of satellite gravity and ship soundings (Tozer et al., 2019), uncertainty is introduced. One source of uncertainty comes from deriving bathymetry from satellite gravity. Satellite-derived bathymetry is limited by the wavelength band resolvable and small seamounts are not resolved (Smith and Sandwell, 1997; Tozer et al., 2019). We constructed a synthetic grid and confirm that, if any, those potentially unresolved small seamounts (height < 1000 m)

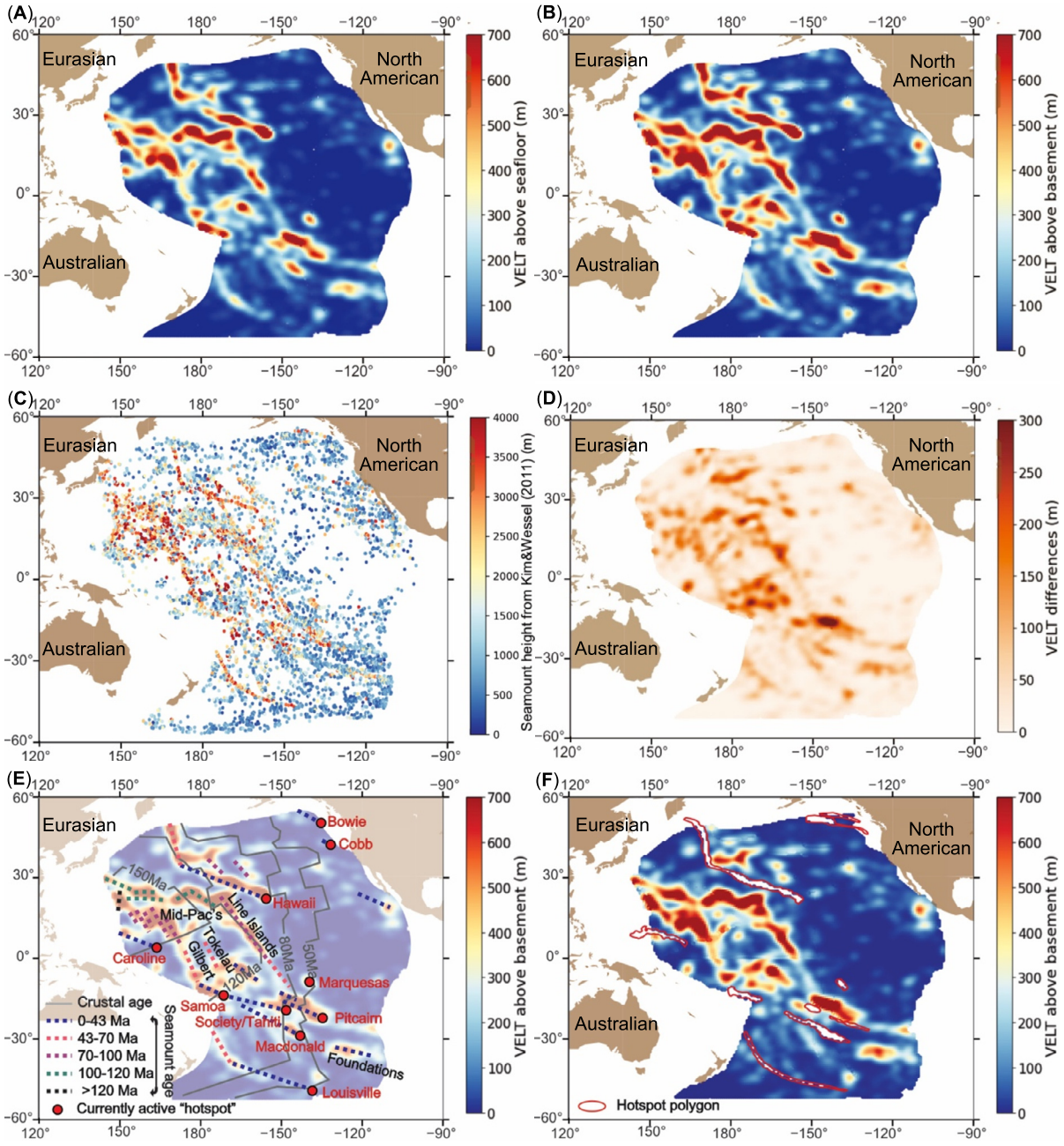

Fig. 2. Spatial distribution of seamount volume represented by volcanic equivalent layer thickness (VELT) of the Pacific plate. (**A**) VELT above seafloor based on exposed seamount topography. (**B**) VELT above basaltic basement after sediment-coverage correction. (**C**) Heights of individual seamounts (Kim and Wessel, 2011). (**D**) Differences between VELT above seafloor (**A**) and VELT above basaltic basement (**B**), i.e. the volume of VELT buried in sediment. (**E**) Seamount chains with age information, selected names (Koppers et al., 2003) and proposed currently active "hotspots" in the Pacific plate (names in red) superposed on the VELT above basaltic basement. (**F**) VELT above basaltic basement excluding the proposed plume-related seamounts (using the list of Courtillot et al., 2003). This panel thus represents VELT from seamounts not proposed to be plume-related and thus generally accepted to be due to plate tectonic processes.

are unimportant in the quantification of seamount volume distribution for the Pacific (Supplementary Fig. S5). In addition, there are misfits between shipboard measurements and satellite-derived bathymetry. For seamounts, the misfits are highly correlated and can be explained to a significant degree by the gravity effect of uncompensated bathymetry (Watts et al., 2020). Uncertainty analysis described in the supplement suggests that when the RMS error of the seamount height is < 500 m, the misfits have a minimal effect on the VELT distribution result (Supplementary Fig. S6). We thus conclude that the distribution of volcanism we calculate based on SRTM15+V2.0 (RMS of ± 180 m, Tozer et al., 2019) is reliable.

3.2. Intraplate volcanism vs. crustal age

Consistent with the map view of the VELT distribution (Fig. 2), the relationship between volume and seafloor age shows that larger volcanic volumes concentrate in older crust (Fig. 3A). Two prominent peaks occur at seafloor ages of ~120 Ma and >~160 Ma. The peak around ~120 Ma corresponds to the Hawaiian-Emperor seamount chain, most of which lies within the Cretaceous magnetic quiet zone (84-124 Ma), the Line islands (emplacement ages of 70-100 Ma) and the Samoan seamounts (emplacement ages of <43 Ma) (Fig. 2E). The other peak at >~160 Ma (Fig. 3A) corresponds to scattered seamounts emplaced at 70-100 Ma (Fig. 2E). From the difference between the crustal and em-

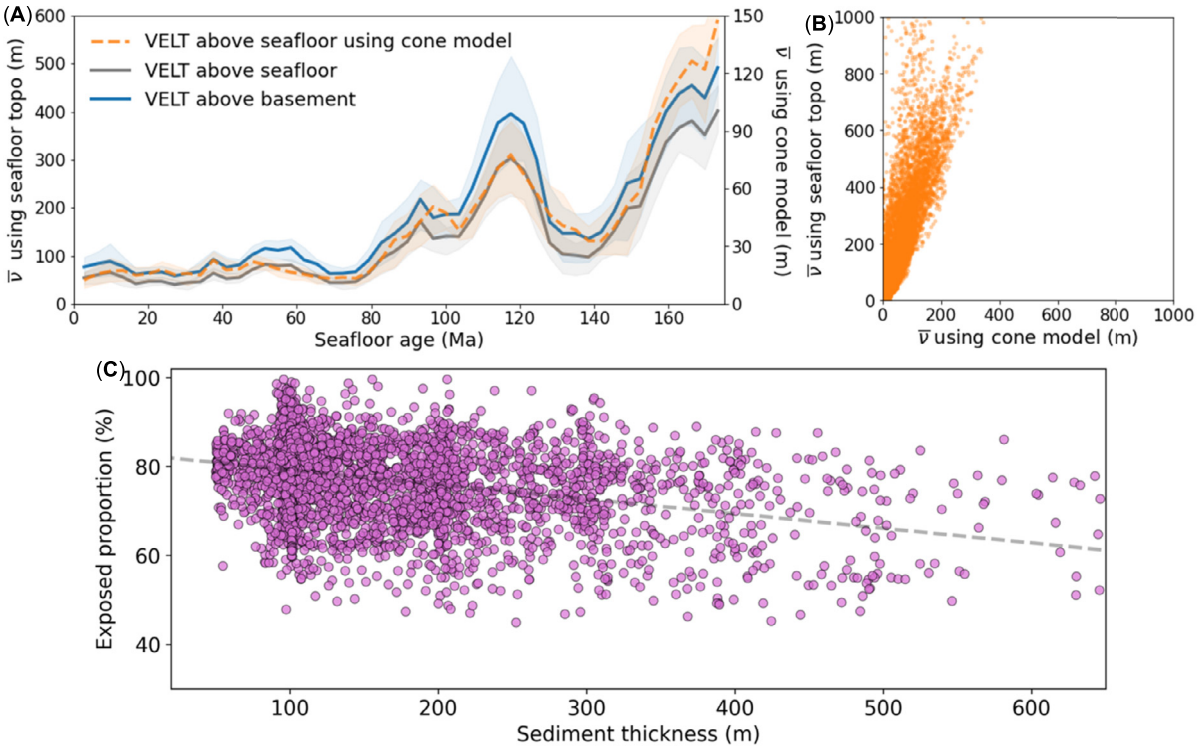

Fig. 3. Seamount volume distribution as a function of seafloor age and its correlation with sediment coverage. (**A**) VELT, $\overline{\nu}$, as a function of seafloor age for the portion of seamounts exposed above the sediment (grey) and after sediment coverage correction (blue), along with $\overline{\nu}$ computed from the database of Kim and Wessel (2011) using an elliptical cone model (orange). Shaded regions indicate half a standard deviation (0.5-σ) and represent the scatter of VELT values per age bin. (**B**) A comparison of $\overline{\nu}$ using above seafloor topography and $\overline{\nu}$ using the cone model. Using the cone model causes great underestimation of seamount volume. (**C**) Proportion of VELT above seafloor as a function of sediment thickness at the same location. Best-fitting distribution (dashed line) shows a generally negative correlation.

placement ages, it can be seen that most of these large seamounts formed on lithosphere that was, at the time of eruption, older than 20 Myr in both near-ridge and off-ridge settings (Watts et al., 1980).

3.3. Volume bias analysis

In order to compare our VELT results to prior work on seamount volume quantification, we also compute $\overline{\nu}$ using the elliptical cone model from the database of Kim and Wessel (2011) (Fig. 3A). We confirm that this yields a total seamount volume vs. seafloor age trend very consistent with our total VELT vs. seafloor age results (Supplementary Fig. S7A). However, $\overline{\nu}$ computed using the cone model is underestimated by 75% (Figs. 3A and 3B) as a result of neglecting irregular shape and sediment blanketing.

Irregular seamount shapes and densely clustered seamount groups in particular cause large biases in computed volume using idealized cone shapes. The proportion of volume exposed above the sediment layer (the ratio of volume above the seafloor to volume above the basaltic basement) mainly falls in the range 60%-85% of total volcanic volume (Fig. 3C). There is a generally negative correlation between exposed VELT proportion and sediment thickness (Fig. 3C). Sediment coverage is a significant confounding factor for quantifying seamount volume.

A bias of 75% is significantly larger than previously reported (Kim and Wessel, 2011). The larger standard deviation (σ) we obtained for $\overline{\nu}$ for seafloor ages >80 Ma (Fig. 3A) is a reflection of the wide range of seamount sizes in the mid-aged and old Pacific.

A striking increase in $\overline{\nu}$ occurs for seafloor ages >140 Ma (Fig. 3A). However, total VELT or total volcanic volume in this age range is low for the oldest Pacific seafloor (Supplementary Fig. S7A) because it is relatively small in area–a large part of Jurassic Pacific seafloor has been subducted. While it is impossible to estimate the subducted Mesozoic seamount volume, we use $\overline{\nu}$ as our comparison metric (as opposed to total volume) to partially account for varying areas within observable seafloor age ranges.

4. Mantle plume influence

4.1. Plume-attributed volcanism distribution

To investigate the contribution of seamounts proposed to arise from mantle plumes, we divide the seamounts into four categories (Table 1). For each category, we compute $\overline{\nu}$ vs. seafloor age (Fig. 4) and the frequency distribution (i.e., histogram) (Fig. 5). First, we compare the chronological distributions of the erupted volumes produced by all seamounts in the Pacific plate (Cat. 1), seamounts not attributed to plumes (Cat. 2), and seamounts that are attributed to plumes (Cat. 3). There is great disagreement among authors concerning which volcanoes are produced by plumes and which are not (Courtillot et al., 2003; Morgan and Morgan, 2007; Sleep, 1990; Torsvik et al., 2006). In this discussion, we use the list of Courtillot et al. (2003) and include their "primary" and "secondary" plumes in Cat. 3 (i.e., 10 plumes). We found that the choice of plume list had little influence on the overall results (Tables 2 and S1, Figs. 4D and S9). VELT is plotted against seafloor age in Fig. 4A and cumulative total volume is shown in Fig. 4B.

The first three $\overline{\nu}$ categories vary synchronously where seafloor age is <140 Ma and show a striking peak at 120 Ma and a minor peak at 90 Ma (Fig. 4A). This tight correlation indicates that the three categories of volcanism have had similar distributions since the Cretaceous. In the oldest oceanic crust (>140 Ma), $\overline{\nu}$ for Cat. 1 and Cat. 2 is greatest while Cat. 3 has very low $\overline{\nu}$ (Fig. 4A). This shows that plume-related volcanism is predicted to account for only a very small fraction of the intraplate volcanism in the older part of the Pacific plate. The plot of cumulative VELT across

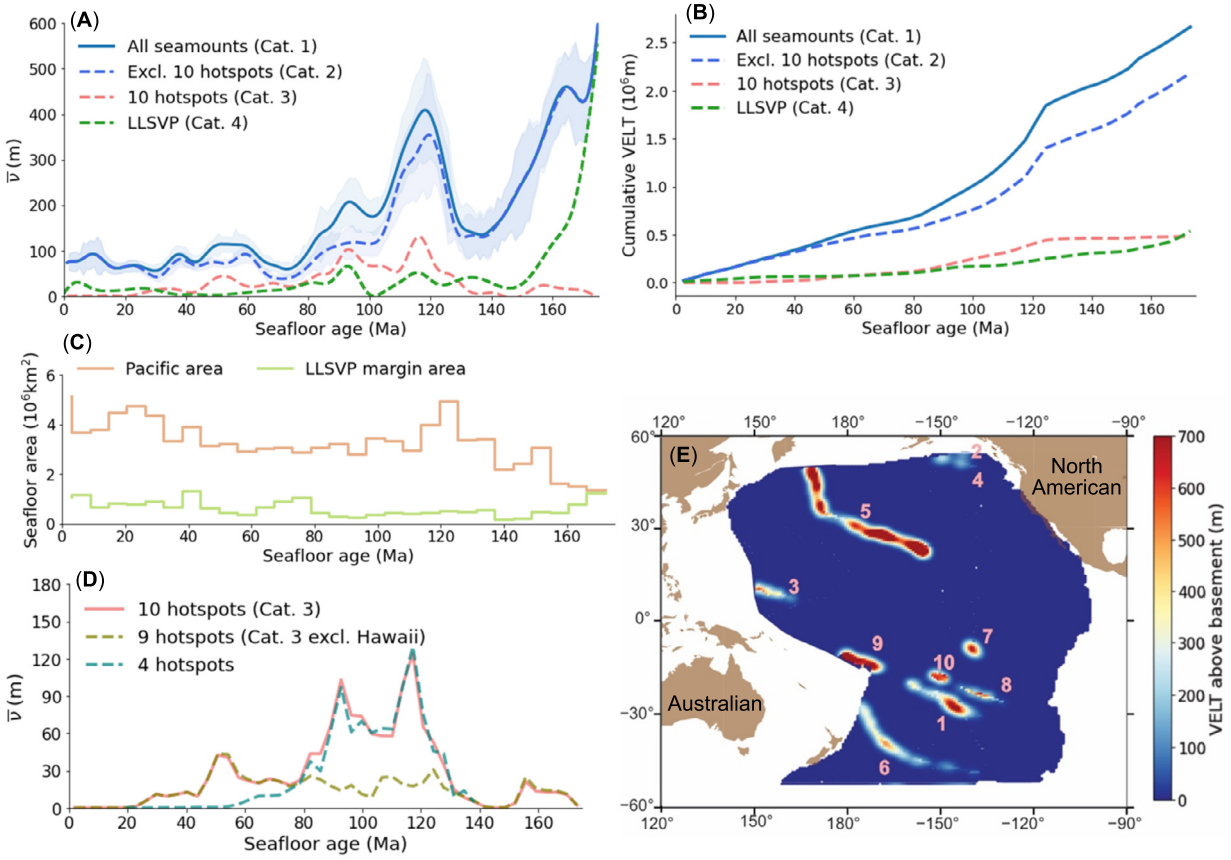

Fig. 4. Comparison of VELT above basaltic basement for four categories of seamounts (Table 1). (**A**) VELT ($\overline{\nu}$) as a function of seafloor age. Shaded regions of $\overline{\nu}$ indicate an uncertainty of 0.5-σ. Cats.1-3 change synchronously where seafloor ages are $<$ 140 Ma; plume-related volcanism accounts for a small fraction of the total where seafloor ages are $<$ 140 Ma. (**B**) Cumulative VELT of plume-related volcanism (Cat. 3) takes up only a small fraction (18%) of the intraplate volcanism in the Pacific plate (Cat. 1). (**C**) Seafloor area of the LLSVP margin and seafloor area of the entire Pacific plate as a function of seafloor age. (**D**) Comparisons of VELT ($\overline{\nu}$) for different plume lists as a function of seafloor age (Table 2). (**E**) VELT above basaltic basement related to proposed-plume seamounts (using the list of Courtillot et al., 2003). Numbering of hotspot corresponds to Table 2. This panel represents VELT produced by proposed plumes.

Table 1
Categories of seamounts in the Pacific plate.

Category number	Description
Cat. 1	All seamounts
Cat. 2	Non-hotspot (non-plume-related) seamounts
Cat. 3	Hotspot (plume-related) seamounts
Cat. 4	All seamounts above LLSVP margin

the entire Pacific (Fig. 4B) further illustrates this point by showing proposed plume volcanism (Cat. 3) only accounts for 18% of the total (Cat. 1). Moreover, plume-attributed products cannot be distinguished from the rest on the basis of frequency distribution of individual seamount volumes (Figs. 5 and S8). The products attributed to plumes and those attributed to non-plume processes essentially form a single statistical population.

4.2. Volcanism distribution above LLSVP margins

The LLSVPs have been proposed to be relatively long-lived, dense bodies in the lower mantle (Lay, 2005). Torsvik et al. (2008) proposed that deep mantle plumes rise from their boundaries, citing as evidence a spatial correlation with large igneous provinces (Bower et al., 2013; Davies et al., 2012; McNamara and Zhong, 2005; Zhang et al., 2010). Old plume products may have been transported away from the LLSVP margin, but our computations show that no recently active hotspot exists above the current LLSVP margin in the oldest seafloor. Here, we compare seamount volcanism above a 1000-km-wide band forming the LLSVP boundary (Cat. 4) and the volume of all seamounts in the Pacific (Cat. 1) (Fig. 4A). The chosen LLSVP boundary corresponds to the seismic velocity anomaly of -1% dln (Vs) in the SMEAN model at 2800 km depth (Becker and Boschi, 2002). In the mid-aged Pacific plate, $\overline{\nu}$ for Cat. 4 changes synchronously with the other three categories with peaks at 90 Ma and 120 Ma. Using different widths for the LLSVP margin gives similar results (Supplementary Fig. S9).

In contrast to the results for plume-related volcanism (Cat. 3), seamounts above the LLSVP margin are highly concentrated in old seafloor with a constant increase of $\overline{\nu}$ for ages $>$150 Ma (Fig. 4A). In the oldest seafloor ($>$170 Ma), almost all of the seamounts are located above the LLSVP margin ($\overline{\nu}$ of Cat. 4 overlaps $\overline{\nu}$ of Cat. 1), which is simply because a large proportion of the old oceanic crust is within our LLSVP margin (Fig. 4C). However, these large values of $\overline{\nu}$ are not associated with proposed plumes (i.e., $\overline{\nu}$ of Cat. 3 stays low), indicating that intraplate volcanism above the current LLSVP margin in the oldest seafloor is mainly sourced by non-plume processes.

The LLSVP margin includes a progressively larger area of the seafloor as it youngs from $\sim$20 Ma to 0 Ma (increasing from 0.8×10^6 km^2 to 1.2×10^6 km^2, Fig. 4C) while the contribution to the total volume of intraplate volcanism made by seamounts on young seafloor stays low. Moreover, there is no intraplate plume in any lists above the LLSVP margin for seafloor $<$ 20 Ma (Fig. 4E). It is generally assumed (though not proven) that the Pacific LLSVP has been stationary relative to the spin axis of the Earth during the past 300 Myr (Torsvik et al., 2008). If this is correct, our results show that, in the last $\sim$20 Ma, intraplate volcanism in the young

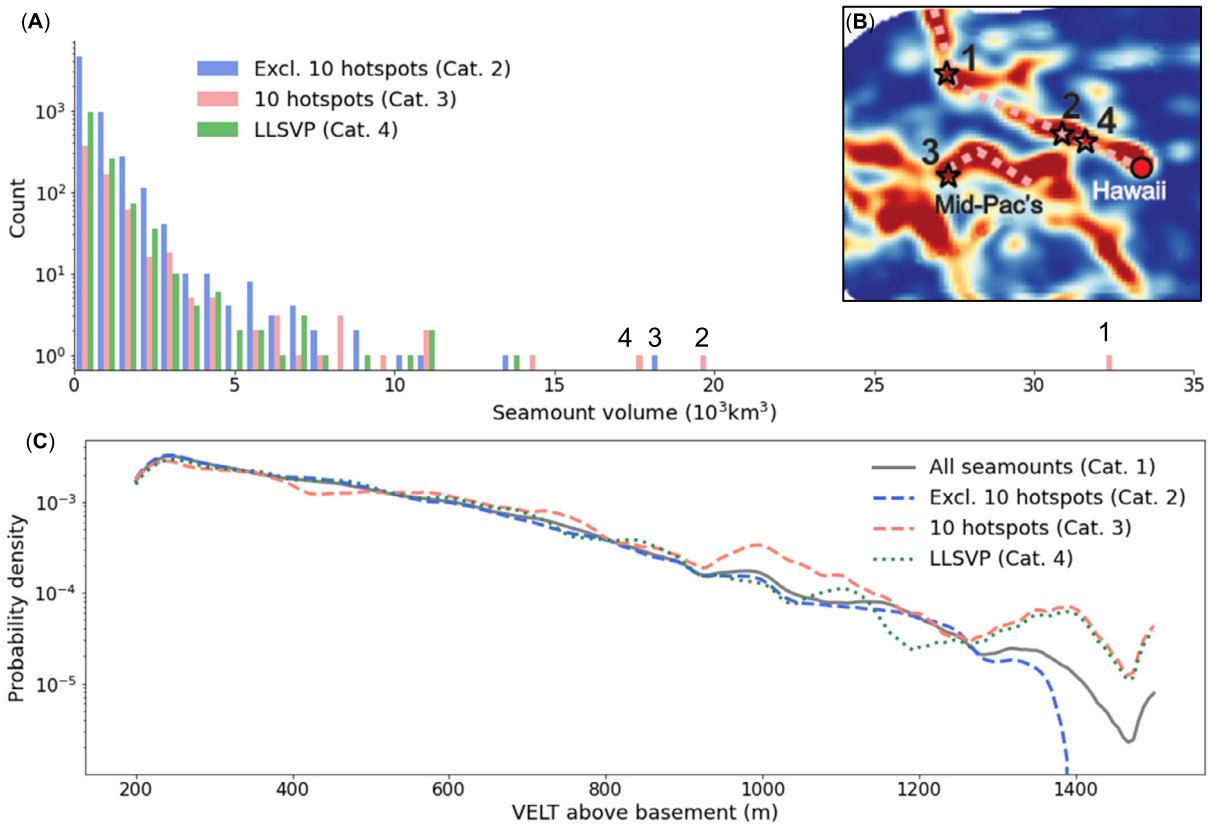

Fig. 5. Frequency distributions (histograms) of different categories of seamounts (Table 1). (**A**) Histogram of individual seamount volumes computed from the database of Kim and Wessel (2011) using the elliptical cone model. (**B**) Locations of the four largest individual seamounts in the database. Three out of four seamounts are located along the Hawaiian-Emperor seamount chain. (**C**) Probability density distributions of VELT for different categories. Different categories of seamounts show similar frequency distributions.

Table 2
Comparison of selected hotspot (plume) lists in the Pacific plate.

	Hotspot (plume) name	Ten hotspots (plume-related seamounts), after Courtillot et al. (2003)	Four hotspots (plume-related seamounts), after Torsvik et al. (2006)	Nine hotspots (plume-related seamounts) for comparison
1	Macdonald (including Maria/Southern Cook, Argo, North Austral)	X		X
2	Bowie-Kodiak	X		X
3	Caroline	X		X
4	Cobb/Jan de Fuca	X		X
5	Hawaii	X	X	
6	Louisville	X	X	X
7	Marquesas	X		X
8	Pitcairn	X		X
9	Samoa	X	X	X
10	Society/Tahiti	X	X	X

crust above the LLSVP margin is mostly contributed by non-plume-related seamounts.

4.3. Volcanism volumes for different plume lists

We also compute plume-related VELT using other lists for the Pacific (Figs. 4D and 4E, Table 2), i.e., nine (Cat. 3 excluding Hawaii), and four (Torsvik et al., 2006). For tests using more lists, see the supplement where we present results for twelve plumes (Morgan and Morgan, 2007) and two "primary" plumes–the Hawaiian-Emperor and Louisville seamount chains–considered by Courtillot et al. (2003) to originate from the core-mantle boundary (Supplementary Table S1, Fig. S8). Notably, the "hotspotting" technique (Wessel and Kroenke, 1997) is effective to map out the potential plume-like upwelling seamounts. The list of hotspots suggested by "hotspotting" method (Wessel et al., 2006) adds three more "hotspots" to the list of Morgan and Morgan (2007) (Supplementary Table S1). However, these additional "hotspots" are likely formed by short-lived and discontinuous intraplate volcanism originating at very shallow mantle depths, which is suggested to be built by regional plate extension (Ito et al., 1995; Koppers and Staudigel, 2005). Therefore, these additional seamount chains are not included in the hotspot category.

Using different plume lists to compute both $\overline{\nu}$ (Fig. 4D) and the probability density distribution of the plume-related VELT (Supplementary Figs. S8A-S8D) gives very similar results. Overall, $\overline{\nu}$ shows that proposed plume-related seamounts are mainly concentrated on mid-aged seafloor (90-120 Ma) except for the seamount volume distribution that excludes Hawaii (Figs. 4D and SE). That is to say, only the Hawaiian seamount chain includes seamounts that produce large enough volumes to significantly change the distribution of proposed-plume-related volcanism in the Pacific plate. Thus, in

this respect, proposed-plume volcanism volume in the Pacific plate is heavily dependent on Hawaii alone.

4.4. Seamount volume histograms

A histogram of individual seamount volumes, based on the database of Kim and Wessel (2011), further distinguishes different kinds of intraplate volcanism (Fig. 5A). The seamounts are divided into those excluding plumes (Cat. 2), those attributed to plumes (Cat. 3), and those above the LLSVP margin (Cat. 4). All three categories show similar exponential distributions for seamount volumes smaller than 15000 km^3 (Fig. 5A). Four outliers have volumes >15000 km^3. Among them, three belong to the Hawaiian-Emperor seamount chain. The other outlier, the SIO Guyot, lies on the westernmost edge of the Mid-Pacific mountains (Nemoto and Kroenke, 1985) (Fig. 5B), which is not considered to be plume-fed (Clouard and Bonneville, 2001; Courtillot et al., 2003). SIO Guyot is an exceptionally large seamount built by non-plume processes. Its large volume, ~18000 km^3, offers some indication of the seamount volumes that researchers accept can be produced without the involvement of mantle plumes.

The spatial density of the VELT grids allows for well-formed histograms that exhibit approximately exponential probability densities for all categories. We further apply a kernel density estimation smoothing operator to the histogram bins to obtain continuous probability curves while maintaining relevant frequency variations (Fig. 5C). Consistent with Fig. 5A, all the probability curves are similar for values of VELT < 900 m. When VELT > 900 m, the curve for Cat. 3 is higher than the other three categories, indicating more large seamounts in the plume category compared with the others. When VELT > 1250 m, the curves of Cats. 3 and 4 are very similar and both are systematically higher than Cats. 1 and 2. This confirms that these large seamounts are systematically interpreted as plume-related. As discussed above (Figs. 4D and 5A), the majority belong to the Hawaiian-Emperor system. Except for these exceptionally large seamounts, in general, the similarity of the probability density curves suggests that on the Pacific plate intraplate volcanism considered to be related to plumes does not have a volume distribution that is significantly different from non-plume volcanism.

5. Discussion and conclusions

The spatial distribution of VELT expresses the supply of melt to Earth's surface. Our results show volcanism proposed to be plume-associated (including both "primary" and "secondary" plumes) only contributes 18% of the volume of total intraplate volcanism (Fig. 4B). Of all proposed plumes in the Pacific plate, Courtillot et al. (2003) consider only Hawaii and Louisville to originate from the lowermost mantle. Other studies have contested this and reject the plume hypothesis entirely (Anderson et al., 2014). Our estimated plume VELT represents an upper bound of the erupted volume attributed to the most widely accepted plumes.

Although different authors have proposed many different plume lists (e.g., Morgan and Morgan, 2007; Torsvik et al., 2006), the volume budget is dominated by the Emperor-Hawaiian system and the inclusion of smaller features does not significantly change the above findings (Figs. 4D and SE). The interaction between mantle plumes and mid-ocean ridges is proposed to have generated massive volumes of melts that is preserved as oceanic plateaus (Madrigal et al., 2016; Taylor, 2006). We manually extracted the bathymetry associated with oceanic plateaus based on the polygons of Madrigal et al. (2016) and computed the VELT contribution (Supplementary Fig. S10). Even considering all of them to be plume-generated, the maximum proportion of plume-related VELT (including ten plume-related seamount chains and oceanic plateaus) is still less than 50% of the total intraplate volcanism.

We also considered an extreme scenario where the oceanic crust is thickened at the base of the plume-related seamounts due to magmatic underplating (Watts and Ten Brink, 1989) but not under non-plume seamounts. For the few seamounts with well-defined crustal structures, the ratios between the volume of intra-crustal magmatic intrusions and extrusive volcanism are 10%-30% (Hawaiian volcanoes; Flinders et al., 2013), ~40% (Hawaii seamount chain; Watts and Ten Brink, 1989), or 53.2% (Louisville seamount chain; Contreras-Reyes et al., 2010). Assuming an end-member scenario where all proposed plume-related seamounts have large intrusive bodies and no non-plume-related ones do, we recompute the VELT distribution by simply multiplying the plume-related VELT by 140% (Supplementary Fig. S11). Results show these intrusive volumes have minor implications for the overall spatial distribution of mean VELT. As for the total volume of seamount volcanism, the fraction of intraplate volcanism from plumes increases from 18% (excluding intrusive bodies) to 23.5% (including intrusive bodies). Therefore, while plumes are proposed to have produced most of the oceanic plateaus and large-sized seamounts, these do not account for the majority of the total observable intraplate volcanism of the Pacific plate.

Similar work by Conrad et al. (2017) proposed that intraplate volcanism is sourced from asthenospheric melts while some local areas with higher volcanism, such as the older Pacific, might require additional melts from the deep mantle. Our accurate mapping of seamount volcanism further clarifies that these postulated additional melts from the deep mantle account for at most 18% of total intraplate volcanism in the Pacific plate. Our results therefore indicate that plume processes do not dominate the intraplate volcanism, the majority of which is likely related to non-plume processes.

The method we used can be expanded to other oceans. Sediment thickness varies more in other oceans (e.g., in the Atlantic, sediment cover ranges from 0 to >1 km; Straume et al., 2019), implying that volcanism has been even more underestimated in these areas. It would also be interesting to perform similar studies for the continents. In this way, investigation into the source of intraplate volcanic activity on Earth can advance.

CRediT authorship contribution statement

Y.Z. devised the project, conducted the computation and analyses, and wrote the original manuscript; B.R. developed the computational framework, performed the numerical calculations, improved writing and wrote the methodology section; G.R. edited the manuscript, provided critical feedback, improved writing and data visualization; W.D. led the funding acquisition, jointly discussed the results and provided suggestions for further improvement of the figures and writing. All authors reviewed the results and approved the final version of the manuscript.

Declaration of competing interest

The authors declare that they have no known competing financial interests or personal relationships that could have appeared to influence the work reported in this paper.

Data availability

Data are archived as described in the acknowledgements.

Acknowledgements

We thank Ling Chen and Lijun Liu for constructive discussions and D. Sandwell and N. Sleep for their helpful reviews. Fig. 1 in this paper was constructed using GMT 6 (Wessel et al., 2019).

Funding: This work was supported by the National Natural Science Foundation of China (No. 41906070, No. 91858214 and No. 42025601), Leading Talents in Scientific and Technological Innovation Project of Zhejiang Province (No. 2019R52034).

Data and materials availability: Bathymetric data are available at https://topex.ucsd.edu/WWW_html/srtm15_plus.html. Sediment thickness data are available at https://www.ngdc.noaa.gov/mgg/sedthick/. Derived VELT grids are available at https://doi.org/10.5281/zenodo.5716540.

Appendix A. Supplementary material

Supplementary material related to this article can be found online at https://doi.org/10.1016/j.epsl.2022.117786.

References

Anderson, D.L., 2000. The thermal state of the upper mantle: no rule for mantle plumes. Geophys. Res. Lett. 27, 3623–3626. https://doi.org/10.1029/2000GL011533.

Anderson, D.L., Natland, J.H., Ernst, W.G., 2014. Mantle updrafts and mechanisms of oceanic volcanism. Proc. Natl. Acad. Sci. USA 111, E4298–E4304. https://doi.org/10.1073/pnas.1410229111.

Ballmer, M.D., van Hunen, J., Ito, G., Tackley, P.J., Bianco, T.A., 2007. Non-hotspot volcano chains originating from small-scale sublithospheric convection. Geophys. Res. Lett. 34, 1–5. https://doi.org/10.1029/2007GL031636.

Becker, T.W., Boschi, L., 2002. A comparison of tomographic and geodynamic mantle models. Geochem. Geophys. Geosyst. 3.

Bonatti, E., Harrison, C.G.A., 1976. Hot lines in the Earth's mantle. Nature 263, 402–404. https://doi.org/10.1038/263402a0.

Bower, D.J., Gurnis, M., Seton, M., 2013. Lower mantle structure from paleogeographically constrained dynamic Earth models. Geochem. Geophys. Geosyst. 14, 44–63.

Clouard, V., Bonneville, A., 2001. How many Pacific hotspots are fed by deep-mantle plumes? Geology 29, 695–698.

Coffin, M.F., Eldholm, O., 1994. Large igneous provinces: crustal structure, dimensions, and external consequences. Rev. Geophys. 32, 1–36.

Conrad, C.P., Bianco, T.A., Smith, E.I., Wessel, P., 2011. Patterns of intraplate volcanism controlled by asthenospheric shear. Nat. Geosci. 4, 317–321. https://doi.org/10.1038/ngeo1111.

Conrad, C.P., Selway, K., Hirschmann, M.M., Ballmer, M.D., Wessel, P., 2017. Constraints on volumes and patterns of asthenospheric melt from the space-time distribution of seamounts. Geophys. Res. Lett. 44, 7203–7210. https://doi.org/10.1002/2017GL074098.

Conrad, C.P., Wu, B., Smith, E.I., Bianco, T.A., Tibbetts, A., 2010. Shear-driven upwelling induced by lateral viscosity variations and asthenospheric shear: a mechanism for intraplate volcanism. Phys. Earth Planet. Inter. 178, 162–175. https://doi.org/10.1016/j.pepi.2009.10.001.

Contreras-Reyes, E., Grevemeyer, I., Watts, A.B., Planert, L., Flueh, E.R., Peirce, C., 2010. Crustal intrusion beneath the Louisville hotspot track. Earth Planet. Sci. Lett. 289, 323–333. https://doi.org/10.1016/j.epsl.2009.11.020.

Courtier, A.M., Jackson, M.G., Lawrence, J.F., Wang, Z., Lee, C.-T.A., Halama, R., Warren, J.M., Workman, R., Xu, W., Hirschmann, M.M., 2007. Correlation of seismic and petrologic thermometers suggests deep thermal anomalies beneath hotspots. Earth Planet. Sci. Lett. 264, 308–316.

Courtillot, V., Davaille, A., Besse, J., Stock, J., 2003. Three distinct types of hotspots in the Earth's mantle. Earth Planet. Sci. Lett. 205, 295–308.

Craig, C.H., Sandwell, D.T., 1988. Global distribution of seamounts from Seasat profiles. J. Geophys. Res., Solid Earth 93, 10408–10420.

Davies, D.R., Goes, S., Davies, J.H., Schuberth, B.S.A., Bunge, H.-P., Ritsema, J., 2012. Reconciling dynamic and seismic models of Earth's lower mantle: the dominant role of thermal heterogeneity. Earth Planet. Sci. Lett. 353, 253–269.

Fairhead, J.D., Wilson, M., 2005. Plate tectonic processes in the South Atlantic Ocean: do we need deep mantle plumes? Spec. Pap., Geol. Soc. Am. 388, 537–553. https://doi.org/10.1130/0-8137-2388-4.537.

Flinders, A.F., Ito, G., Garcia, M.O., Sinton, J.M., Kauahikaua, J., Taylor, B., 2013. Intrusive dike complexes, cumulate cores, and the extrusive growth of Hawaiian volcanoes. Geophys. Res. Lett. 40, 3367–3373. https://doi.org/10.1002/grl.50633.

Foulger, G.R., Natland, J.H., 2003. Is "hotspot" volcanism a consequence of plate tectonics? Science 80. https://doi.org/10.1126/science.1083376.

Gans, K.D., Wilson, D.S., Macdonald, K.C., 2003. Pacific Plate gravity lineaments: diffuse extension or thermal contraction? Geochem. Geophys. Geosyst. 4.

Hieronymus, C.F., Bercovici, D., 1999. Discrete alternating hotspot islands formed by interaction of magma transport and lithospheric flexure. Nature 397, 604–607. https://doi.org/10.1038/17584.

Hirano, N., Takahashi, E., Yamamoto, J., Abe, N., Ingle, S.P., Kaneoka, I., Hirata, T., Kimura, J.-I., Ishii, T., Ogawa, Y., Machida, S., Suyehiro, K., 2006. Volcanism in response to plate flexure. Science 80.

Ito, G., McNutt, M., Gibson, R.L., 1995. Crustal structure of the Tuamotu Plateau, 15°S, and implications for its origin. J. Geophys. Res. 100, 8097–8114. https://doi.org/10.1029/95JB00071.

Kim, S.S., Wessel, P., 2011. New global seamount census from altimetry-derived gravity data. Geophys. J. Int. 186, 615–631. https://doi.org/10.1111/j.1365-246X.2011.05076.x.

Kitchingman, A., Lai, S., Morato, T., Pauly, P., et al., 2007. How many seamounts are there and where are they located. In: Seamounts Ecol. Conserv. Manag. Fish Aquat. Resour. Ser. Blackwell, Oxford.

Koppers, A.A.P., Staudigel, H., 2005. Asynchronous bends in Pacific seamount trails: a case for extensional volcanism? Science 80 (307), 904–907. https://doi.org/10.1126/science.1107260.

Koppers, A.A.P., Staudigel, H., Pringle, M.S., Wijbrans, J.R., 2003. Short-lived and discontinuous intraplate volcanism in the South Pacific: hot spots or extensional volcanism? Geochem. Geophys. Geosyst. 4, 1089. https://doi.org/10.1029/2003GC000533. 10.

Lau, H.C.P., Mitrovica, J.X., Davis, J.L., Tromp, J., Yang, H.-Y., Al-Attar, D., 2017. Tidal tomography constrains Earth's deep-mantle buoyancy. Nature 551, 321–326.

Lay, T., 2005. The deep mantle thermo-chemical boundary layer: the putative mantle plume source. In: Foulger, G.R., Natland, J.H., Presnall, D.C., Anderson, D.L. (Eds.), Plates, Plumes, and Paradigms. Geological Society of America, Boulder, CO, pp. 193–206.

Madrigal, P., Gazel, E., Flores, K.E., Bizimis, M., Jicha, B., 2016. Record of massive upwellings from the Pacific large low shear velocity province. Nat. Commun. 7, 1–12. https://doi.org/10.1038/ncomms13309.

Matheron, G., Serra, J., 1988. Strong Filters and Connectivity. Image Analysis and Mathematical Morphology. Academic Press, London.

McNamara, A.K., Zhong, S., 2005. Thermochemical structures beneath Africa and the Pacific Ocean. Nature 437, 1136–1139.

Meyer, F., 1979. Iterative image transformations for an automatic screening of cervical smears. J. Histochem. Cytochem. 27, 128–135.

Morgan, W.J., 1971. Convection plumes in the lower mantle. Nature 230, 42–43.

Morgan, W.J., Morgan, J.P., 2007. Plate velocities in the hotspot reference frame. In: Foulger, G.R., Jurdy, D.M. (Eds.), Plates, Plumes, and Planetary Processes. Geological Society of America, Boulder, CO, pp. 65–78.

Nemoto, K., Kroenke, L.W., 1985. Sio Guyot: a complex volcanic edifice in the western Mid-Pacific Mountains. Geo Mar. Lett. 5, 83–89.

Phipps Morgan, J., Morgan, W.J., Zhang, Y., Smith, W.H.F., 1995. Observational hints for a plume-fed, suboceanic asthenosphere and its role in mantle convection. J. Geophys. Res., Solid Earth 100, 12753–12767.

Rasmussen, C.E., 2003. Gaussian processes in machine learning. In: Summer School on Machine Learning. Springer, pp. 63–71.

Seton, M., Müller, R.D., Zahirovic, S., Williams, S., Wright, N.M., Cannon, J., Whittaker, J.M., Matthews, K.J., McGirr, R., 2020. A global data set of present-day oceanic crustal age and seafloor spreading parameters. Geochem. Geophys. Geosyst. 21, e2020GC009214.

Sleep, N.H., 1997. Lateral flow and ponding of starting plume material. J. Geophys. Res., Solid Earth 102, 10001–10012.

Sleep, N.H., 1990. Hotspots and mantle plumes: some phenomenology. J. Geophys. Res., Solid Earth 95, 6715–6736.

Smith, W.H.F., Sandwell, D.T., 1997. Global sea floor topography from satellite altimetry and ship depth soundings. Science 80 (277), 1956–1962. https://doi.org/10.1126/science.277.5334.1956.

Straume, E.O., Gaina, C., Medvedev, S., Hochmuth, K., Gohl, K., Whittaker, J.M., Abdul Fattah, R., Doornenbal, J.C., Hopper, J.R., 2019. GlobSed: updated total sediment thickness in the world's oceans. Geochem. Geophys. Geosyst. 20, 1756–1772.

Stuart, W.D., Foulger, G.R., Barall, M., 2007. Propagation of the Hawaiian-Emperor volcano chain by Pacific plate cooling stress. Spec. Pap., Geol. Soc. Am. 430, 497–506. https://doi.org/10.1130/2007.2430(24).

Taylor, B., 2006. The single largest oceanic plateau: Ontong Java-Manihiki-Hikurangi. Earth Planet. Sci. Lett. 241, 372–380. https://doi.org/10.1016/j.epsl.2005.11.049.

Torsvik, T.H., Burke, K., Steinberger, B., Webb, S.J., Ashwal, L.D., 2010. Diamonds sampled by plumes from the core-mantle boundary. Nature 466, 352–355.

Torsvik, T.H., Smethurst, M.A., Burke, K., Steinberger, B., 2008. Long term stability in deep mantle structure: evidence from the ~300 Ma Skagerrak-Centered Large Igneous Province (the SCLIP). Earth Planet. Sci. Lett. 267, 444–452.

Torsvik, T.H., Smethurst, M.A., Burke, K., Steinberger, B., 2006. Large igneous provinces generated from the margins of the large low-velocity provinces in the deep mantle. Geophys. J. Int. 167, 1447–1460.

Tozer, B., Sandwell, D.T., Smith, W.H.F., Olson, C., Beale, J.R., Wessel, P., 2019. Global Bathymetry and Topography at 15 Arc Sec: SRTM15+. Earth Sp. Sci. 6, 1847–1864. https://doi.org/10.1029/2019EA000658.

Tripathi, N.K., Gokhale, K.V.G.K., Siddiqui, M.U., 2000. Directional morphological image transforms for lineament extraction from remotely sensed images. Int. J. Remote Sens. 21, 3281–3292. https://doi.org/10.1080/014311600750019895.

Vogt, T., Del Valle, H.F., 1994. Calcretes and cryogenic structures in the area of Puerto Madryn (Chubut, Patagonia, Argentina). Geogr. Ann., Ser. A, Phys. Geogr. 76, 57–75.

Watts, A.B., Bodine, J.H., Ribe, N.M., 1980. Observations of flexure and the geological evolution of the Pacific Ocean basin. Nature 283, 532–537.

Watts, A.B., Ten Brink, U.S., 1989. Crustal structure, flexure, and subsidence history of the Hawaiian Islands. J. Geophys. Res. 94. https://doi.org/10.1029/jb094ib08p10473.

Watts, A.B., Tozer, B., Harper, H., Boston, B., Shillington, D.J., Dunn, R., 2020. Evaluation of shipboard and satellite-derived bathymetry and gravity data over Seamounts in the Northwest Pacific Ocean. J. Geophys. Res., Solid Earth 125, 1–18. https://doi.org/10.1029/2020JB020396.

Wessel, P., 1997. Sizes and ages of seamounts using remote sensing: implications for intraplate volcanism. Science 80. https://doi.org/10.1126/science.277.5327.802.

Wessel, P., 2001. Global distribution of seamounts inferred from gridded Geosat/ERS-1 altimetry. J. Geophys. Res., Solid Earth 106, 19431–19441. https://doi.org/10.1029/2000JB000083.

Wessel, P., Harada, Y., Kroenke, L.W., 2006. Toward a self-consistent, high-resolution absolute plate motion model for the Pacific. Geochem. Geophys. Geosyst. 7, 1–23. https://doi.org/10.1029/2005GC001000.

Wessel, P., Kroenke, L., 1997. A geometric technique for relocating hotspots and refining absolute plate motions. Nature 387, 365–369.

Wessel, P., Luis, J.F., Uieda, L., Scharroo, R., Wobbe, F., Smith, W.H.F., Tian, D., 2019. The Generic Mapping Tools version 6. Geochem. Geophys. Geosyst. 20, 5556–5564. https://doi.org/10.1029/2019GC008515.

Wessel, P., Sandwell, D.T., Kim, S.S., 2010. The global seamount census. Oceanography 23, 24–33. https://doi.org/10.5670/oceanog.2010.60.

Wilson, J.T., 1966. Did the Atlantic close and then re-open? Nature 211, 676–681. https://doi.org/10.1038/211676a0.

Wilson, J.T., 1963. A possible origin of the Hawaiian Islands. Can. J. Phys. 41, 863–870.

Yesson, C., Clark, M.R., Taylor, M.L., Rogers, A.D., 2011. The global distribution of seamounts based on 30 arc seconds bathymetry data. Deep-Sea Res., Part 1, Oceanogr. Res. Pap. 58, 442–453. https://doi.org/10.1016/j.dsr.2011.02.004.

Zhang, N., Zhong, S., Leng, W., Li, Z.-X., 2010. A model for the evolution of the Earth's mantle structure since the Early Paleozoic. J. Geophys. Res., Solid Earth 115.

Zhao, C., Garnero, E.J., McNamara, A.K., Schmerr, N., Carlson, R.W., 2015. Seismic evidence for a chemically distinct thermochemical reservoir in Earth's deep mantle beneath Hawaii. Earth Planet. Sci. Lett. 426, 143–153.

Zhao, Y., Ding, W., Yin, S., Li, J., Zhang, J., Ding, H., 2020. Asymmetric post-spreading magmatism in the South China Sea: based on the quantification of the volume and its spatiotemporal distribution of the seamounts. Int. Geol. Rev. 62, 955–969.